IOP Publishing New J. Phys. 26 (2024) 023008 https://doi.org/10.1088/1367-2630/ad21b7

New Journal of Physics
The open access journal at the forefront of physics

Deutsche Physikalische Gesellschaft DPG
IOP Institute of Physics

Published in partnership with: Deutsche Physikalische Gesellschaft and the Institute of Physics

OPEN ACCESS

RECEIVED
3 March 2023

REVISED
17 January 2024

ACCEPTED FOR PUBLICATION
23 January 2024

PUBLISHED
7 February 2024

Original Content from this work may be used under the terms of the Creative Commons Attribution 4.0 licence.

Any further distribution of this work must maintain attribution to the author(s) and the title of the work, journal citation and DOI.

PAPER

Exploring the quantum vacuum via ultraintense laser-induced refraction of light

J Wang[1,6], G Y Chen[1,6], B F Lei[1,*], S Jin[1], L Y Yang[1,6], L F Gan[1], C T Zhou[1,2], S P Zhu[3,4], X T He[1,3] and B Qiao[1,5,*]

[1] School of Physics, Center for Applied Physics and Technology, HEDPS, and SKLNPT, Peking University, Beijing 100871, People's Republic of China
[2] Center for Advanced Material Diagnostic Technology, Shenzhen Technology University, Shenzhen 518118, People's Republic of China
[3] Institute of Applied Physics and Computational Mathematics, Beijing 100094, People's Republic of China
[4] Graduate School of China Academy of Engineering Physics, PO Box 2101, Beijing 100088, People's Republic of China
[5] Frontiers Science Center for Nano-optoelectronic, Peking University, Beijing 100094, People's Republic of China
[6] These authors contributed equally to this work
[*] Authors to whom any correspondence should be addressed.

E-mail: bqiao@pku.edu.cn and blei@pku.edu.cn

Keywords: vacuum refraction, high intensity laser beam, vacuum polarization, particle in cell simulation

Abstract

The rapid progress of ultraintense laser technology provides a novel route to explore the quantum vacuum effect in the laboratory. Here, we propose using oblique collisions between an ultraintense pump laser and an x-ray probe laser to experimentally identify the quantum vacuum effect, where the change of the refraction properties including the refraction angle of the probe laser is taken as a detectable signature. The theoretical basis of the proposed scheme are analyzed in details, where a reasonable estimation of the scheme is given. To verify the proposed scheme, a series of two-dimensional particle-in-cell (PIC) simulations, with the vacuum polarization effect self-consistently taken into account, are carried out.

1. Introduction

With the rapid development of ultrashort and ultraintense lasers promoted by the chirped pulse amplification (CPA) technique [1], upcoming high power laser facilities such as the Extreme Light Infrastructure [2], Vulcan [3], and SULF [4] are expected to produce laser pulses with unprecedented peak intensities up to 10^{23}–$10^{25}\,\mathrm{W\,cm^{-2}}$. This opens up a new opportunity for the experimental exploration of strong field quantum electrodynamics (QED), such as the vacuum polarization phenomenon which has been studied through strong magnetic field excitation for over 20 years [5–10]. These experiments are considered to be one of the most important applications of high power laser facilities.

A foreseeable prospect is proposed with the medium-like properties of quantum vacuum routing from the prediction by Euler and Heisenberg that vacuum can be polarized by electromagnetic (EM) field [11, 12]. Various optical effects excited by ultraintense lasers have aroused people's interest in theoretical and experimental exploration such as vacuum diffraction [13], double-slit interference [14], Bragg Scattering [15], photon splitting and merging [16], high order harmonic generation [17], vacuum reflection [18, 19], etc [20–22]. Related theoretical researches and methodologies are continuously being refined like high order corrections [23], vacuum emission picture [24, 25] and etc [20, 26]. It is noted that certain astronomical systems, such as neutron stars, are surrounded by magnetic fields close to the Schwinger field. These extremely strong fields lead to significant effects related to vacuum polarization [27, 28], such as vacuum birefringence [29–31], photon splitting [32], and etc [33, 34]. More importantly, together with the advancement in modern optical detection system, many of these effects have the potential to be detected in experiments. For example, the vacuum birefringence effect has recently attracted great research interest [13, 35–38] and the on-going project FOR2783 in Germany aims to achieve the first proof-of-principle XFEL and birefringence-based experiment [37, 39, 40]. Meanwhile, one may anticipate that the vacuum refraction is

© 2024 The Author(s). Published by IOP Publishing Ltd on behalf of the Institute of Physics and Deutsche Physikalische Gesellschaft

also one of the basic and critical effects of this vacuum medium [41]. Additionally, it provides an alternative method for detecting quantum vacuums as the precision of beam angle measurements advances to the nano-radian scale and further [42, 43]. Some early attempts to study vacuum refraction signals can be found in [44, 45]. There is further research including an experiment (named DeLLight) which is under development at Université Paris-Saclay (France) recently [46]. However, a careful theoretical estimation, simulations and particularly a feasible refraction-based schemes with ultraintense lasers for quantum vacuum probing, require further exploration.

In this paper, we propose a scheme to explore the quantum vacuum effect on ultraintense laser facilities, in which an x-ray probe laser is applied to obliquely collide with the ultraintense pump laser, shown schematically in figure 6(a). The theoretical basis of the scheme is analyzed, where the wavefront expansion method is used to consider the potential detectable signals in refraction-based experiments, including the refraction angle, the change of the intensity of the refraction beam and the difference between the direction of energy propagation and wavefront propagation (called walk-off effect). To verify the proposed scheme, we carry out a series of two-dimensional (2D) particle-in-cell (PIC) simulations with modeling of the quantum vacuum polarization effect self-consistently included. The simulation results have confirmed that the generalized Snell's and Fresnel's law can be used as a reasonable description of the refraction of the probe laser for most of the settings that can be employed experimentally today. A complete simulation shows that the refraction angle in our scheme is on the order of nrad. This angle, which serves as a detectable signature of the quantum vacuum, can be measured under realistic parameters in current experiments. We believe these results can provide an intuitive guidance to the potential experimental scheme based on quantum vacuum refraction driven by intense laser, while ensuring that important influencing factors are not lost.

2. Theoretical analysis

Vacuum polarization leads to interactions between photons in vacuum. This phenomenon was first described by Heisenberg and Euler using an QED effective Lagrangian density $\mathcal{L}_{\rm eff} = \mathcal{L}_{\rm cl} + \mathcal{L}_{\rm HE}$ [11, 47, 48], where $\mathcal{L}_{\rm cl} = -\varepsilon_0(\mathbf{E}^2 - c^2\mathbf{B}^2)/2$ is the classical Lagrangian density, ε_0 is the vacuum permittivity, and $\mathcal{L}_{\rm HE}$ is the effective correction to $\mathcal{L}_{\rm cl}$. According to the Euler–Lagrange equation for EM fields, this effective correction further results in QED modified Maxwell's equations. In these equations, the superposition principle of EM fields no longer holds and the interaction between them can be included by the nonlinear polarization vectors $\mathbf{P}$ and magnetization vectors $\mathbf{M}$ of quantum vacuum. In the regime of slow-varying perturbative weak-field, where $\omega \ll \omega_c$, $E \ll E_{\rm cr}$ and $B \ll B_{\rm cr}$ fulfilled by the state-of-the-art high-intensity lasers, the leading contribution of $\mathbf{P}$ and $\mathbf{M}$ are given as [49, 50]:

$$\mathbf{P} \simeq 2\xi\left[2\left(\mathbf{E}^2 - c^2\mathbf{B}^2\right)\mathbf{E} + 7c^2\left(\mathbf{E}\cdot\mathbf{B}\right)\mathbf{B}\right],$$

$$\mathbf{M} \simeq -2\xi c^2\left[2\left(\mathbf{E}^2 - c^2\mathbf{B}^2\right)\mathbf{B} - 7\left(\mathbf{E}\cdot\mathbf{B}\right)\mathbf{E}\right]. \tag{1}$$

The nonlinear coupling parameter of vacuum polarization is given by $\xi = 2\alpha^2\varepsilon_0^2\hbar^3/45m_e^4c^5 \sim 1.3\times10^{-52}$, where α is the fine structure constant, $\omega_c = m_ec^2/\hbar$ is the Compton frequency, the QED critical field $E_{\rm cr} = m_e^2c^3/e\hbar \simeq 1.32\times10^{18}\,\mathrm{V\,m^{-1}}$.

2.1. Quantum refraction

According to equation (1), a single (paraxial) laser beam as considered for the probe fulfills both $\mathbf{E}^2 - c^2\mathbf{B}^2 = 0, \mathbf{E}\cdot\mathbf{B} = 0$. This makes $\mathbf{P}, \mathbf{M} = 0$, so the probe beam can return to be governed by the classical Maxwell's Lagrangian, which We call propagating in free vacuum. However, if a strong background pump field exists simultaneously, the properties of the vacuum are modified significantly by the the polarization of vacuum $\mathbf{P}, \mathbf{M}$, which is called quantum vacuum.

We begin our analysis with a relatively general scenario. Set a strong EM field as the pump field, of $\mathbf{E}_{s,y} = E_s(\mathbf{r},t)\hat{y}$ and $\mathbf{B}_{s,z} = -B_s(\mathbf{r},t)\hat{z}$, where $E_s = cB_s$. Such a pump field allows both temporal and spatial variations, and can describe a strong laser field by selecting an appropriate profile distribution. Consider a laser pulse as a probe beam with, $\mathbf{E}_p = E_p(\mathbf{r},t)\hat{z}$ and $\mathbf{B}_p = B_{p,y}(\mathbf{r},t)\hat{y} - B_{p,x}(\mathbf{r},t)\hat{x}$ propagates through a quantum vacuum polarized by this strong pump EM field. In this paper, we call the probe wave with the electric field always in the z direction the S-polarized wave, and the one with $\mathbf{E}$ in the $x-y$ plane the P-polarized wave. Due to the similarity between the two, we give only the analysis of the S-wave in detail, and present the results of the P-wave when appropriate. Here, $\mathbf{r} = (x,y,z)$ is the vector of spatial coordinate, and $E_p \ll E_s$. Our theoretical analysis does not rely on the specific modeling of the probe laser. The pump fields here and in later simulations need to fulfill $\mathbf{E}^2 - c^2\mathbf{B}^2 = 0, \mathbf{E}\cdot\mathbf{B} = 0$, otherwise the vacuum polarization effect of the pump field itself may mask the signal we need. By substituting them into equation (1), the quantum nonlinear polarization and magnetization are obtained as

$$P_z = 14\xi c^2 \left(-E_s B_{p,y} + B_s E_p\right) B_s,$$
$$M_y = 14\xi c \left(E_s B_{p,y} - B_s E_p\right) E_s. \tag{2}$$

Here the other components P_y and M_z can be neglected for the probe beam propagation, beacause $P_y, M_z \sim \mathcal{O}(E_s E_p^2) \ll P_z, M_y \sim \mathcal{O}(E_s^2 E_p)$. According to the QED modified Maxwell's equation, the spatial-temporal evolution of E_p can be described by $\partial_t^2 E_p = c^2 \nabla^2 E_p - \partial_t^2 P_z/\varepsilon_0 - \partial_x \partial_t M_y/\varepsilon_0$. The behavior near the laser wavefront can be studied by the following asymptotic expansion: $E_p = \Sigma_n \phi_n f_n(s) = \Sigma_n \phi_n f_n(t - \sigma(\mathbf{r}))$, where the lowest order term ϕ_0 determines the electric field strength of the wavefront of the laser. f_n usually does not need to be explicitly determined as long as it can make the expansion converge and $f_n'(s) = f_{n-1}(s)$ is satisfied [51]. $s = t - \sigma(\mathbf{r})$ is eikonal and defines how the wavefront (surface $s(\mathbf{r}, t) =$ constant or $\sigma(\mathbf{r}) =$ constant) moves in $\mathbf{r}$ space. Substituting this series into the evolution equation, and equating the coefficients of the successive f_n to zero, we get,

$$1 - c^2 (\nabla\sigma)^2 + cA_s (\partial_x \sigma) + c^2 A_s (\partial_x \sigma)^2 + A_s + cA_s \partial_x \sigma = 0, \tag{3}$$

where $A_s = 14\xi E_s^2/\varepsilon_0$ and $\nabla = (\partial_x, \partial_y, \partial_z)$. Equation (3) is the important starting point for our analysis of wavefront and refraction properties. We give a brief derivation and analysis of the formula in appendix A. In short, although the equation (3) does not depend on the specific form of f_n, the expansion coefficients ϕ and the convergence range do. If the power series expansion (equation (A.6)) is applied, equation (3) is generally valid under the constraint of short distance. If the high-frequency expansion (equation (A.7)) is applied, equation (3) is valid at least within the range of the variation scale of the pump field being much larger than that of the probe. However, in more general cases, it is difficult to give a general valid range in theory, and using simulations to verify applicability is a more convenient method.

Equation (3) is an anisotropic partial differential equation and can be converted into a set of characteristic equations as follows

$$\frac{\mathrm{d}x}{\mathrm{d}\lambda} = -2c^2 (\partial_x \sigma) + \left(2A_s c + 2A_s c^2 (\partial_x \sigma)\right), \tag{4}$$
$$\frac{\mathrm{d}y}{\mathrm{d}\lambda} = -2c^2 \left(\partial_y \sigma\right), \tag{5}$$
$$\frac{\mathrm{d}p_x}{\mathrm{d}\lambda} = -\partial_x A_s \left(2\partial_x \sigma + (\partial_x \sigma)^2 + 1\right), \tag{6}$$
$$\frac{\mathrm{d}p_y}{\mathrm{d}\lambda} = -\partial_y A_s \left(2\partial_x \sigma + (\partial_x \sigma)^2 + 1\right). \tag{7}$$

Equations (4)–(7) are a set of ordinary differential equations where $p_x = \partial_x \sigma$, $p_y = \partial_y \sigma$ represent the normal direction of wavefront. Substituting the equations (4) and (5) and (∂_x (equation (3))) into $\frac{\mathrm{d}p_x}{\mathrm{d}\lambda} = (\partial_x p_x)\frac{\mathrm{d}x}{\mathrm{d}\lambda} + (\partial_y p_x)\frac{\mathrm{d}y}{\mathrm{d}\lambda}$ can get equation (6). A similar operation on $\frac{\mathrm{d}p_y}{\mathrm{d}\lambda}$ yields equation (7). So, equations (3)–(7) are self consistent. If we set the initial x, y (and p_x, p_y) to be a point on the wavefront, the curve given by these equations can describe the spatial trajectory of that point as it changes with the parameter λ. This trajectory actually represents the direction of energy transport. If we drop the second term in equation (4), the 'velocity' of x, y of the new trajectory only depends on the wavefront normal, i.e. the orthogonal trajectory of the wavefront. The difference between two directions can be referred to as wake-off angel. Given an initial wavefront, traversing the points on the wavefront to get a cluster of orthogonal trajectories gives the evolution of the whole wavefront. The difference between the direction of energy and wavefront propagation comes from the anisotropy introduced by the second term in equation (4).

Equations (4)–(7) indicate that the propagation of the probe beam depends on the pump field configuration including field strength A_s and inhomogeneity ∇A_s. The phase velocity can be calculated from the definition of $s = t - \sigma(\mathbf{r})$ as $v_{ph} = 1/\sqrt{p_x^2 + p_y^2}$. As a result, an effective refractive index (RI), here referred as quantum RI, is given as $n_{\mathrm{qed}} = c\sqrt{p_x^2 + p_y^2}$.

Equations (4)–(7) are sufficient for us to theoretically predict the change in angle during vacuum refraction. Based on this result, some simple cases can be reduced to concise physical pictures. The first one is that a probe beam propagates along $\hat{\mathbf{x}}$-axis in a static uniform pump field $E_{s,y}(\mathbf{r}, t) = E_{s0} =$ const, $B_{s,z}(\mathbf{r}, t) = B_{s0} =$ const. Then, $p = p_x$, equations (6) and (7) indicate that p_x remains constant and the RI of the quantum vacuum can be obtained as

$$n_{\mathrm{qed},s0} = \frac{1 + A_{s0}}{1 - A_{s0}}, \tag{8}$$

where $A_{s0} = A_s|_{E_s=E_{s0}} > 0, n_{\mathrm{qed},s0} > 1$. Similarly, for the P-polarized probe beam, $n_{\mathrm{qed},p0} = (1+A_{p0})/(1-A_{p0})$ where $A_{p0} = 8\xi E_{s0}^2/\varepsilon_0$. The difference between A_{s0} and A_{p0} presents the vacuum birefringence effect. Secondly, an inhomogeneous pump field can lead to the variation of quantum RI and then the appearance of the refraction and reflection as the probe beam passing through. Now, we assume a probe beam propagating along $\hat{x}$-axis into the quantum vacuum pumped by an EM field of a spatial gradient along an arbitrary direction, e.g. of an angle θ_i with respect to $\hat{x}$-axis. From equations (6) and (7), the component of $\vec{p}$ in the direction perpendicular to θ remains invariant. So, at an arbitrary position $(x,y) = (x_m, y_m)$ in the pump field, since $n_{\mathrm{qed}} = c\sqrt{p_x^2 + p_y^2}$, it is expected that there is a local constraint similar to Snell's formula:

$$n_i \sin(\theta_i) = \left(n_{\mathrm{qed},m} + \Delta n_m\right) \sin(\theta_i + \Delta\theta_m). \tag{9}$$

Here we have assumed that the local effective RI is the effective RI in static filed

$$n_{\mathrm{qed},m} = \frac{1+A_m}{1-A_m}, \tag{10}$$

plus a correction. Substituting the assumption equation (9) into equation (3) gives the final result

$$\Delta n_m = \frac{\Delta\theta_m^2}{1 - A_m - A_m/cn_{\mathrm{qed},m}}. \tag{11}$$

Here, $A_m = A_s(x_m, y_m)$ is calculated by the local pump field $E_m = E_s(x_m, y_m)$, and n_i the RI at incident point. $\Delta\theta_m$ is the deflection angle of the wavefront normal at this point with respect to incident angle θ_i and approximately equals to $\Delta\theta_m \simeq \arctan(p_y/p_x) - \theta_i$. It is easy to see that Δn_m and then the local deflection angle $\Delta\theta_m$ are determined only by the local and initial pump and probe field configuration. This implies that the direction of the wave front is independent on the transition path and can be determined locally. If the pump field is smooth or not very strong, e.g. in currently available laboratory condition, the correction of RI in equation (11) is very small, $\Delta n_m \ll 1$, and can be neglected. It should be considered in the case of the extremely strong pump field or of a long propagation distance, e.g. in astronomic environments. For example, research [29] investigated the polarized thermal emission from x-ray faint isolated neutron stars and focused on the impact of vacuum polarization on radiation polarization. Polarization changes are introduced in the ray propagation path by calculating the accumulated vacuum birefringence effect. Finally, if the gradient of the pump field is infinite, an interface is formed (as shown by the solid gray line in figure 1). Refraction reflection can occur at the interface, then equation (9) is reduced to the Snell's equation.

In the previous paragraph, we have discussed the propagation of the wavefront(p_x, p_y). We now focus on the trajectory of energy propagation given by equations (4) and (5). The difference between them (walk-off angle) can be obtained as

$$\begin{aligned}\delta\theta_m = \theta_{\mathrm{wavefront}} - \theta_{\mathrm{energy}} &= \arctan\left(\frac{p_y}{p_x}\right) - \arctan\left(\frac{-2c^2(p_y)}{-2c^2(p_x) + (2A_s c + 2A_s c^2(p_x))}\right) \\ &\sim \frac{p_y\left(2A_s c + 2A_s c^2(p_x)\right)}{-2c^2\left(p_y^2 + p_x^2\right)}.\end{aligned} \tag{12}$$

In principle, since equation (12) is of the same order of magnitude as the $\Delta\theta_m$, it needs to be considered. However, the walk-off effect mainly occurs in the interaction between the probe laser and the pump laser. In the experiment, as the probe laser will eventually leave the pump laser, $\delta\theta_m$ will gradually turn to 0. We make a simple estimation of the impact. Walk-off effect cause an offset between the trajectory of the wavefront normal and the energy, estimated to be $\delta\theta_m \cdot L$. Assume the spatial variation scale of the pump field is λ_P and then the intensity difference between the two trajectories is about $\frac{\delta\theta_m \cdot L}{\lambda_P}$. On the other hand, from equations (6) and (7), the final angle of the probe laser after transmission depends on the pump field intensity (or A_s) on the trajectory. In the experimental configuration where the pump laser and probe laser collide, the value $\frac{\delta\theta_m \cdot L}{\lambda_P}$ is significantly less than 1, indicating the walk-off effect can be largely neglected. However, for experiments with longer interaction distances, such as PVLAS [6], which utilize strong magnetic fields to induce vacuum polarization, the effective distance L over 10^4 m could lead to an accumulation of the walk-off effect. There, given some special setups or designs, it is worthwhile to further explore this phenomenon. Experimental methods of detecting the deflection angle of the probe is usually based on interference technique which involves the information of both the refraction angle and the intensity of the electric field. In general cases, the evolution of the intensity requires additional introduction of the corresponding equation of f_{-1} term in the wavefront expansion method. We are going to adopt a more intuitive approach below.

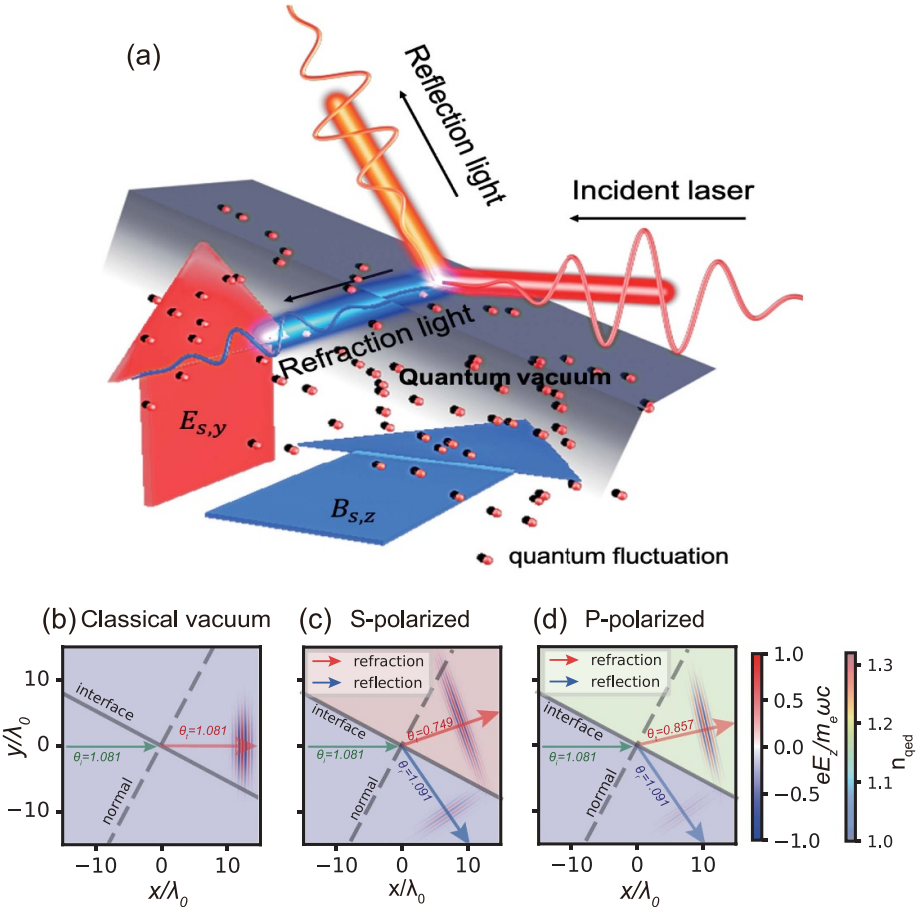

Figure 1. (a) Schematic of refraction and reflection occurring during the transition of the probe from free vacuum to quantum vacuum. Quantum vacuum (gray-colored region) is pumped by a strong EM field and probed by a relatively weak laser pulse (red beam) incident from free into quantum vacuum. Free vacuum here is referred as the vacuum without pump field. (b) PIC result: no refraction and reflection of the probe photon beam happens when it propagates in free vacuum. (c) and (d) PIC results: as transiting into quantum vacuum (regions colored by light red and green) pumped by static field $\mathbf{E}_s, \mathbf{B}_s$, both *S*- and *P*- polarized probe beams reflect and refract similarly with classical optics which can be described by Snell's law. In (b)–(d), the free vacuum is the region colored by gray and the interface is indicated by the solid gray line. The incident direction and position of the probe beam is by green line with an arrow. The detail of the PIC configuration is discussed in section 3.

2.2. Intensity of refracted and reflected light

In general, refraction and reflection happens during a transition process where the RI varies, for example, when passing through an interface of free and quantum vacuum. Therefore, the reflection and refraction can be analyzed in more details with the boundary conditions of the EM fields by the QED modified Maxwell's equations: $\mathbf{e}_n \times (\mathbf{E}_2 - \mathbf{E}_1) = 0$, $\mathbf{e}_n \times (\mathbf{H}_2 - \mathbf{H}_1) = 0$, $\mathbf{e}_n \cdot (\mathbf{D}_2 - \mathbf{D}_1) = 0$ and $\mathbf{e}_n \cdot (\mathbf{B}_2 - \mathbf{B}_1) = 0$, where $\mathbf{H} = \mathbf{B}/\mu_0 - \mathbf{M}$ and $\mathbf{D} = \varepsilon_0\mathbf{E} + \mathbf{P}$. The angles of reflection θ_r and refraction θ_t can be calculated by the Snell's law approximately with the incident angle θ_i as

$$\theta_r = \theta_i\,, \tag{13}$$

$$\theta_t = \arcsin\left(\sin\theta_i/n_{\mathrm{qed},s}\right), \tag{14}$$

where, $n_{\mathrm{qed},s}$ is the quantum RI for *S*-polarized probe pulse. We drop m in equation (10) for convenience. All angles are relative to the normal of the interface at the point of incidence.

From the geometry on the interface of quantum and free vacuum, the amplitudes of magnetic (B) and electric (E) fields of incidence(i), reflection(r) and refraction(t) are related by

$$\frac{B_i}{\mu_0}\cos\theta_i - \frac{B_r}{\mu_0}\cos\theta_r = \frac{B_t}{\mu_0}\cos\theta_t - |M_y|\cos\theta_i \tag{15}$$

$$E_i + E_r = E_t \tag{16}$$

where $M_y = -14\xi c^2[E_sB_t\cos(\theta_i - \theta_t) + B_sE_t]E_s$ is obtained by substituting EM fields in quantum vacuum in equation (1). It is worth mentioning that $M_z = -14\xi c^2[E_sB_t\cos(\theta_i - \theta_t) + B_sE_t]E_t \ll M_y$ is ignored since

$E_t \ll E_s$. By combining equations (15) and (16), the reflectivity and transmittance can be derived in form of Fresnel equations

$$R_{s,r} = \frac{E_r}{E_i} = \frac{\cos\theta_i - C_s}{\cos\theta_i + C_s}, \tag{17}$$

$$R_{s,t} = \frac{E_t}{E_i} = \frac{2\cos\theta_i}{\cos\theta_i + C_s}, \tag{18}$$

where $B_i = E_i/c$, $B_r = E_r/c$ and $B_t = n_{\mathrm{qed},s}E_t/c$ are applied, $C_s = n_{\mathrm{qed}}\cos\theta_t - n_{\mathrm{qed},s}\frac{14\xi E_s^2}{\varepsilon_0}\cos\theta_i - \frac{14\xi E_s^2}{\varepsilon_0}\cos\theta_i$. Bewared that $R_{s,r} < 0$ implies that there is a half wave loss from the reflected wave.

For a P-polarized probe laser, the relationship of EM fields of incidence, reflection and refraction is expressed as

$$E_i\cos(\theta_i) - E_r\cos(\theta_r) = E_t\cos(\theta_t) \tag{19}$$

$$\frac{B_i}{\mu_0} + \frac{B_r}{\mu_0} = \frac{B_t}{\mu_0} - |M_z| \tag{20}$$

where $M_z = 8\xi cE_s^2[E_t\cos(\theta_i - \theta_t) + cB_t]$. Similarly, the reflectivity and transmittance can also be obtained by

$$R_{p,r} = \frac{E_r}{E_i} = \frac{C_p\cos\theta_i - \cos\theta_t}{C_p\cos\theta_i + \cos\theta_t}$$

$$R_{p,t} = \frac{E_t}{E_i} = \frac{2\cos\theta_i}{C_p\cos\theta_i + \cos\theta_t} \tag{21}$$

where $C_p = n_{\mathrm{qed},p}(1 - \frac{8\xi E_s^2}{\varepsilon_0}) - \frac{8\xi E_s^2}{\varepsilon_0}\cos(\theta_i - \theta_t)$.

3. PIC simulation results

In this section we carry out self-consistent simulations to discuss the vacuum refractive behavior under pump fields with different characteristics. To make theoretical estimation intuitive and understandable, and more importantly to check the valid range of our theoretical estimation, we would like to start from an ideal configuration and gradually bring the pump field closer to a real strong laser.

The basic simulation geometry of the pump and probe field is shown in figures 1(c) and (d). The probe beam propagates along $\hat{x}$ axis and intersects the boundary of the pump field with angle θ_i. The simulation box has a size of $30\,\mu\mathrm{m} \times 40\,\mu\mathrm{m}$, and a resolution of $1\,\mu\mathrm{m}/50$ was utilized in both directions. The probe laser pulse is assumed as paraxial gaussian beam with strength $a_p = e|E_p|/m_e\omega_0 c = e|B_s|/m_e\omega_0 = 1$, ω_0 is the laser frequency and the wavelength is $\lambda_p = \lambda_0 = 2\pi c/\omega_0 = 1\,\mu\mathrm{m}$. The peak intensity $I_p = 1.38 \times 10^{18}\,\mathrm{W\,cm^{-2}}$. The temporal profile is also Gaussian with the duration $\tau = 5.6\,\mathrm{fs}$ and the laser is focused at the center $x = 0$ with the waist $r_p = 4\lambda_0$. The amplitude of the pump field is $a_s = 1000$. Because $a_p \ll a_s$, the effect of the probe laser acts on the pump field can be neglected. The nonlinear parameter ξ is artificially increased to be 8.6×10^{-45} in order to more clearly display the reflection and refraction caused by vacuum polarization in our simulations [52]. The rationality of this operation and some implementation details of our simulation program are shown in appendix B.

Firstly, the pump field is configured to be uniform with a sharp boundary separating the free and quantum vacuum. There are two reasons for this setting: 1. We are very familiar with the physical picture, light refracts and changes in intensity at the surface (hard boundary) of a uniform medium. By analogy, it is also the simplest and purest (without other effects) case in which vacuum refraction occurs. 2. There will be no hard boundaries under currently available laboratory conditions. The experimental scheme bases on intense lasers which satisfy the premise $\omega \ll \omega_c$ of our theory. So although the hard boundary breaks this assumption, we can still consider only the leading order contribution to the vacuum refraction and ignore the higher-order corrections [23]. It's natural for us to study this situation first, and then gradually make the pump field more complex to highlight the different core influencing factors respectively.

In current case, as shown in figures 1(c), (d) and 2, the theoretical predictions from equation (9) agree well with PIC results for both *S*- and *P*-polarized probe beam. For example, in the case with *S*-polarized probe beam, the angles of reflection and refraction are $\theta_{r,s} = \pi - \theta_i + \arctan(k_{y,r}/k_{x,r}) = 1.091\ \mathrm{rad} \simeq \theta_i$ and $\theta_{t,s} = \theta_i - \arctan(k_{y,t}/k_{x,t}) = 0.749\ \mathrm{rad} \simeq \sin\theta_i/n_{\mathrm{qed},s0}$, respectively. The normalized peak intensity of electric field of refraction and reflection from PIC are $|\tilde{E}_{z,t,s}|_{\mathrm{PIC}} = 0.7367$ and $|\tilde{E}_{z,r,s}|_{\mathrm{PIC}} = 0.2636$, while the theoretical predictions from equation (18) gives $|\tilde{E}_{z,t,s}|_{\mathrm{theo.}} = 0.7173$ and $|\tilde{E}_{z,r,s}|_{\mathrm{theo.}} = 0.2826$, respectively. For *P*-polarized case, $|\tilde{E}_{z,t,p}|_{\mathrm{PIC}} = 0.8146$ and $|\tilde{E}_{z,r,p}|_{\mathrm{PIC}} = 0.1859$ corresponds to the theoretical predictions

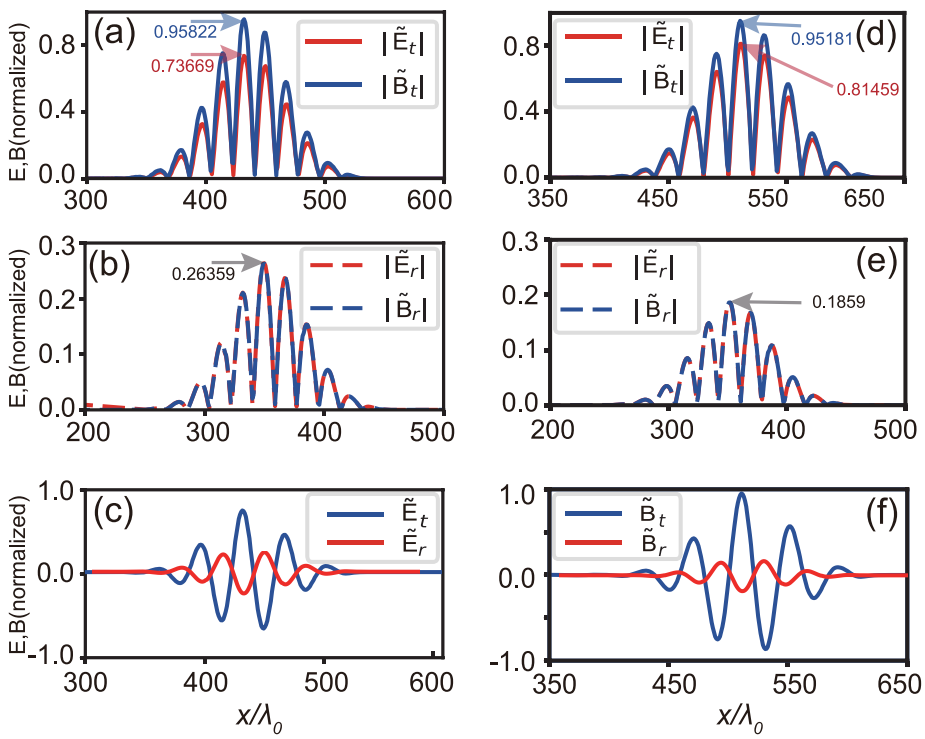

Figure 2. PIC results: (a) and (b): distribution of absolute value of transmitted and reflected electric and magnetic field of the probe beam, calculated as $|\tilde{F}_t| = \sqrt{F_{y,t}^2 + F_{x,t}^2}$ and $|\tilde{F}_r| = \sqrt{F_{y,r}^2 + F_{x,r}^2}$, where $\tilde{F}$ presents either $\tilde{E}$ or $\tilde{B}$ normalized by $m_e c\omega_0/e$ or $m_e\omega_0/e$, respectively. (c) Transmitted (blue) and reflected (red) electric field shows the half wave loss. (d)–(f) With *P*-polarized probe beam, it gives the similar results respectively. The PIC configuration is the same as figures 1(c) and (d).

from equation (21) as $|\tilde{E}_{z,t,p}|_{\text{theo.}} = 0.832$ and $|\tilde{E}_{z,r,p}|_{\text{theo.}} = 0.1662$, respectively. The half wave loss of the reflected pulse is shown in figure 2(c) for *S*-polarized case and in (f) for *P*-polarized case, same as what classical optics predicts. This result may have potential application prospects.

As seen from equations (18) and (21), the reflection and refraction mainly depends on the incident angle θ_i and pump field strength a_s. Therefore, a series of 2D simulations have been performed both for *S*-polarized and *P*-polarized probe lasers as shown in figure 3 where $\theta_r = \theta_i$ is always satisfied. It shows that the larger incident angle leads to the larger refractive angle and reflectivity, but smaller transmittance. Refractive angle, refractivity and transmittance decreasing with a_s presents the fact that stronger pump field results in the lower phase velocity of probe beam. It can be understood that higher intensity EM field can pump higher density of quantum fluctuation and then can promise the better detectable signal in experiments.

Secondly, previous works have used RI derived from a uniform static EM field, similar to equation (10). Since the strong pump field is provided by the high-power laser pulse in experiment, the probe laser experience the periodic variation of the 'vacuum medium' while crossing by. As mentioned in [53], it is necessary to correct the quantum RI and the light cone condition [54] if the spatiotemporal variation of the pump field is considered self-consistently in mathematics. Although equations (3)–(7) and the derived generalized Snell's formula are applicable to pump fields with temporal and spatial variations, their valid range still needs to be verified through simulation. So, we perform the simulation where the pump field varies with time, see figure 4. Based on the previous pump field setup, time modulation is added to the uniform electric field. In order to help guide experiments related to refraction, we gradually increased the oscillation frequency of the pump field. We present a complete comparison of theoretically predicted wavefronts and the simulation results in figure 4. Figures 4(a)–(d) correspond to pump fields with oscillation frequencies $0, \omega_0/20, \omega_0/10, \omega_0/4$, respectively. The black circles in the figure 4 show the wavefront calculated from theoretical prediction, which is in good agreement with the simulation results.

Thirdly, we are going to study the cases where there is spatial variation in the pump field. Here we perform simulations using a quarter-cycle laser field configuration $E_s = E_0 \cos(\pi x/2w_0)$ with a step boundary at $x = 0$, as shown in figure 5(a). We vary w_0 by three different values $w_0 = 1, 2, 4\,\mu$m which is equivalent to controlling the wavelength of the probe laser relative to the pump laser. The probe beam is incident with an angle θ_i with respect to the boundary. The other parameters are the same as above in figure 2. The trajectory of the probe beam in *xy*-plane is plotted for each value of w_0 in figure 5(a) and

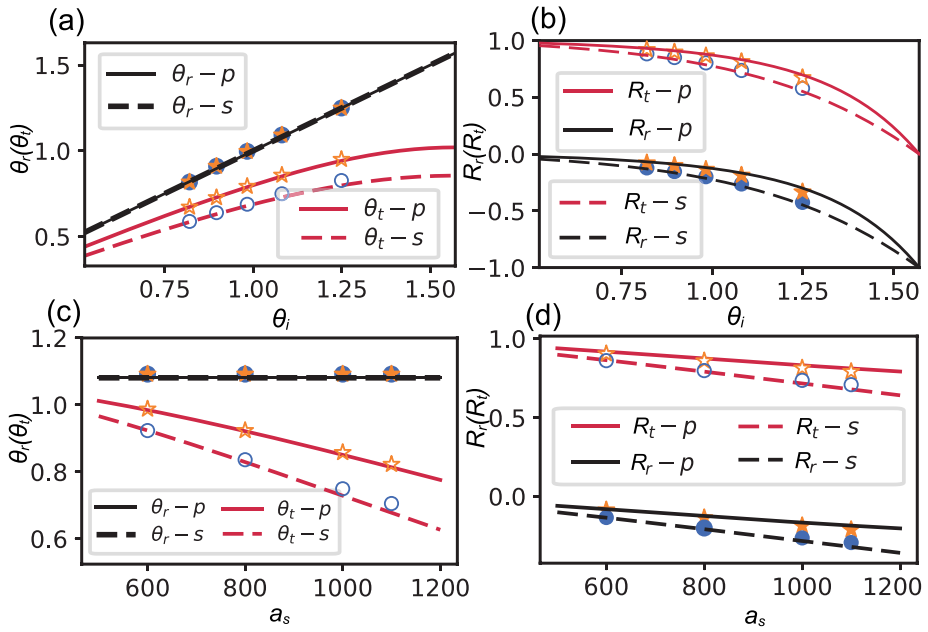

Figure 3. Study of how the deflection and refraction angles, and the reflectivity and transmittance of the probe beam depends on the incident angle θ_i (in (a) and (b)) and pump field strength a_s (in (c) and (d)). Dash and solid lines in each plot presents theoretical predictions for *S*- and *P*-polarized probe lasers while blue and orange stars or circles correspond to the simulation results, respectively. Red and black lines indicate the refracted and reflected beams respectively. In (a) and (b) the angle θ_i is varied as $0.820, 0.896, 0.983, 1.081, 1.249$ rad while $a_s = 1000$. In (c) and (d) a_s varies as $600, 800, 1000, 1100$ while $\theta_i = 1.081$ rad.

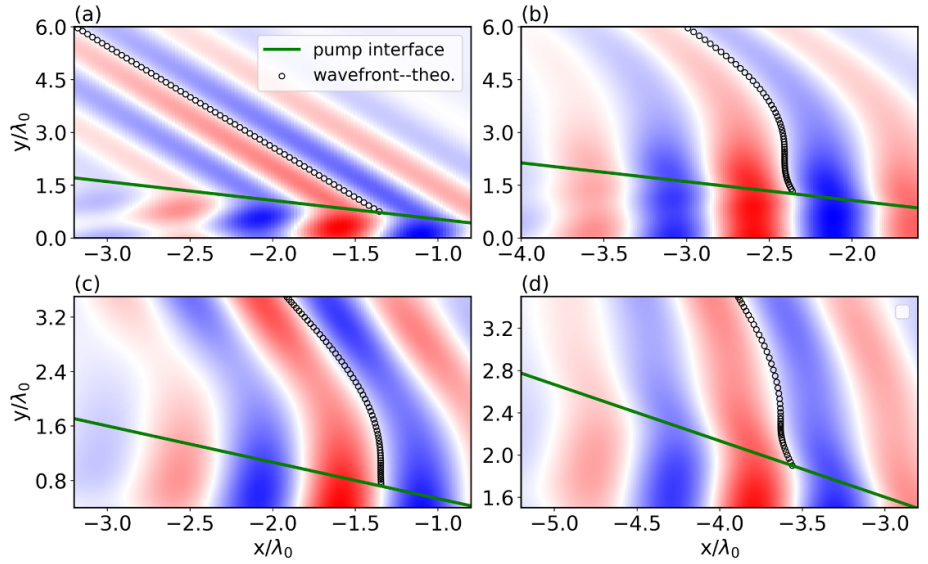

Figure 4. Field ditribution of the probe laser when it propgates in a time varing pump filed. (a)–(d) correspond to the the pump field $E_s = E_0\cos(\omega t)$ with $\omega = 0, \omega_0/20, \omega_0/10, \omega_0/4$, respectively. We take the points with an electric field intensity of 0 as the wavefront of the probe laser (white area). The black circle represents the theoretical wavefront calculated from equations(6) and (7).

compared with the theoretical prediction given by the full description in equations (4)–(7) and by the Snell's formula in equation (14). The difference between the two theories is very small. And the outgoing beams remain parallel in all three w_0 values. This is consistent with the prediction in equation (12). The short wavelength of the pump field, comparable to that of probe beam, does not add additional corrections to analytical results, especially RI, which is different from [53]. Hence, Snell's formula in equation (14) is still a good approximation as expected in section 2.

Furthermore, in real experiments, the relative size of the probe laser to that of the pump field is another critical factor that may have a significant impact. We configure our simulations with a spatial Gaussian profile $E_s = E_0\exp(-r^2/w_0^2)$, as shown in figure 5(b), to study this factor. w_0 is the RMS size of the field. A

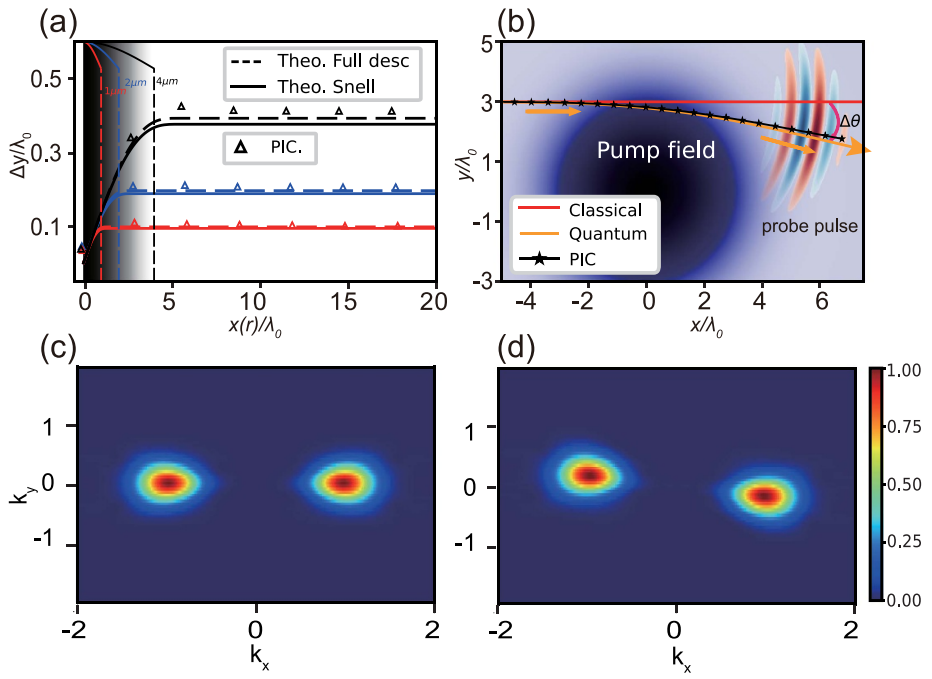

Figure 5. (a) Theoretical (dashed and solid lines) and numerical (triangle) results of transverse offset of the probe beam while passing through quantum vacuum pumped by a quarter-cycle laser pulse (grey region), $E_s = E_0 \cos(\pi x/2w_0)$, $0 < x < w_0$. The probe beam is incident with an angle θ_i. Three dashed vertical lines show the positions where the field drops to 0 for three different values of $w_0 = 1, 2, 4\,\mu$m. The results for the three cases are indicated by different colors: red, blue and black respectively. Since the left and right boundary of the pump field is parallel, the outgoing direction of the probe beam is also parallel to the incident and thus refraction gives a transverse offset Δy. (b) A Gaussian laser pulse (red–blue color map) is incident from left at $y = 3\lambda_0$ and refracted as passing through quantum vacuum (blue region) pumped by a spatial Gaussian field. The solid red line shows the trajectory of the probe beam as propagating in free vacuum. The numerical trajectory (black line with stars) from PIC agrees well with the theoretical prediction (orange line with arrow). (c) and (d) k-space of the probe beam as propagating through the free and quantum vacuum after $t = 10T_0$.

tightly focused Gaussian probe laser pulse of spotsize 1 μm propagates from left and begins to deflect when the local pump field strength E_s is sufficient to give a large quantum RI. As it passes through, the probe beam is significantly refracted with an angle $\Delta\theta$ as shown in figure 5(d). In principle, the theory presented in section 2 allows us to treat the different points on the wavefront of the probe beam as independently propagating rays. The inhomogeneous field results in varying deflection angles at different points, leading to a distorted pulse wavefront. It may also result in a deviation of the PIC trajectory from the theoretical prediction calculated from equation (12). However, it should be very small and can be neglected if the crossing section is relatively small. The trajectory from PIC agrees well with the theoretical prediction as shown in figure 5(b) and only a slight pulse wavefront distortion is observed as shown in figure 5(d). Because the above two simulation parameters, such as wavelength of 1 μm and spotsize of 3 μm, are close to the real parameters of modern ultraintense laser facilities [2–4], these results confirm that our analytical results give reasonable predictions over a wide range of experimental parameter regime.

4. Exploration of quantum vacuum properties using ultraintense laser and x-ray

Now we demonstrate a feasible experimental setup by 2D PIC simulations where a soft x-ray pulse is used as the probe and a high intensity laser pulse as the pump. It is expected that the deflection of propagation direction and the change of intensity can be used as detectable signals. The simulation scheme is shown in figure 6(a). From the above analysis, we can easily see that if two laser beams collide head-on, due to the symmetry in geometric, the propagation direction of the probe laser is collinear with the gradient direction of the pump laser intensity, making it difficult to generate refraction. So we let the two pulses collide at angle θ_c. The pump laser is polarized in $\hat{y}$ direction with peak intensity $I_s = 1.99 \times 10^{24}\,\mathrm{W\,cm^{-2}}$ or $a_s = eE_y/m_e\omega_0 c = 1200$, wavelength $\lambda_0 = 1\,\mu$m, 16th-order super-Gaussian temporal and spatial profile with duration $\tau_s = 10\,$fs and focus radius $r_s = 4\lambda_0$. It is incident from the right boundary with an angle of $\theta_c = 0.489\,$rad into the $4\lambda_0 \times 6\lambda_0$ simulation box consisting of 2000×2500 cells. After time delay of $4T_0$, where $T_0 = \lambda_0/c$, the S-polarized x-ray probe beam with wavelength $\lambda_p = 0.1\lambda_0$, intensity $I_p = 1.38 \times 10^{18}\,\mathrm{W\,cm^{-2}} \ll I_s$ or $a_p = eE_z/2\pi m_e T_0 c = 1$, focus radius $r_p = 3\lambda_p$ and Gaussian temporal profile of RMS duration $\tau_p = 5\,$fs is incident from the left boundary at $y = 0.5\lambda_0$. It crosses the pump field from side

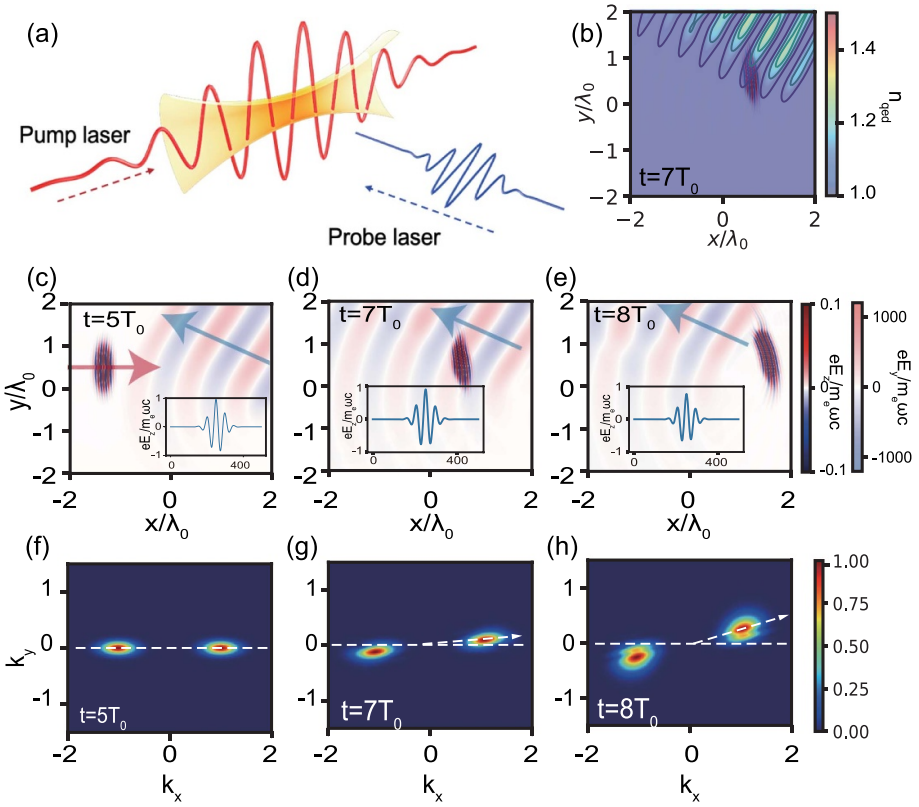

Figure 6. (a) Schematic of the x-ray-laser collision scheme for exploring vacuum polarization. A short x-ray pulse as a probe beam collides with laser pulse as pump field with an angle. (b) The quantum vacuum shows a spatial and temporal distribution depending on the strong pump field. (c)–(e) Field distribution of probe and pump laser pulse at three different time $t = 5T_0$, $7T_0$ and $8T_0$. The refraction effect can clearly shown in k-space in (f)–(h) respectively. Here, amplitude of the reflected beam is too small to be seen here.

similarly as shown in figure 5(b). Note that $\xi = 8.6 \times 10^{-45}$ remains in simulation for clarity of demonstration, but all explicit values given below have been rescaled back to real-world physical values.

The distribution of quantum RI calculated with the help of equation (10) is shown in figure 6(b), and indicates that the structure of quantum vacuum totally depends on the pump field. While colliding with the pump laser at an angle, the x-ray pulse traverses obliquely over the quantum vacuum with $n_{\rm qed} > 1$, and can be expected to be deflected away from its initial propagation path. The electric field distributions of pump laser (E_y) and probe x-ray (E_z) at $t = 5T_0, 7T_0, 8T_0$ are shown in figures 6(c)–(e) respectively. The corresponding K-space distributions of x-ray probe are also presented in figures 6(f)–(h) respectively. The deflection angle is $\phi = 0.239 \times 1.52 \times 10^{-8}$ rad and the strength of probe x-ray is reduced to $a_{p,f} = 0.77 \times 1.52 \times 10^{-8}$ after passing through at $8T_0$, corresponding the theoretical predictions of $\phi = 0.196 \times 1.52 \times 10^{-8}$ rad and $a_{p,f} = 0.64 \times 1.52 \times 10^{-8}$ by equations (9)–(18). The small difference comes from the spatial and temporal field distribution. The dependence of the deflection angle on the collision angle and pump field strength is studied as shown in figure 7. The deflection angle ϕ increases with a_s and decreases with θ_c, which can be scaled approximately with Snell's law in equation (9) as $\phi \sim \theta_i - \arcsin(\cos\theta_c / n_{\rm qed})$, where $\theta_i = \pi/2 - \theta_c$.

Under the real experimental conditions, the simple scaling law for estimating refractive angle can be given as $\phi \approx 2.52 \times 10^{-9} \cdot (I_s/[1.38 \times 10^{24}\,{\rm W\,cm^{-2}}])$ rad. Assuming the intensity of the pump laser is $I_s = 1.38 \times 10^{24}\,{\rm W\,cm^{-2}} (a_s = 1000)$, where the condition of $I_s \ll I_{cr}$ is satisfied and other parameters of lasers are the same as those in figure 6, the deflection angle of the probe x-ray is estimated to be $\phi \sim 2$ nrad after passing through. This small deflection is enough to realize interferometric measurement by changing the interference fringe. The state-of-art interferometry, which proposed for the ultra precise measurement of the small laser angular deflection, can provide the resolution on the single $n$rad-level and extremely robust and insensitive to the most common disturbances [42, 43].

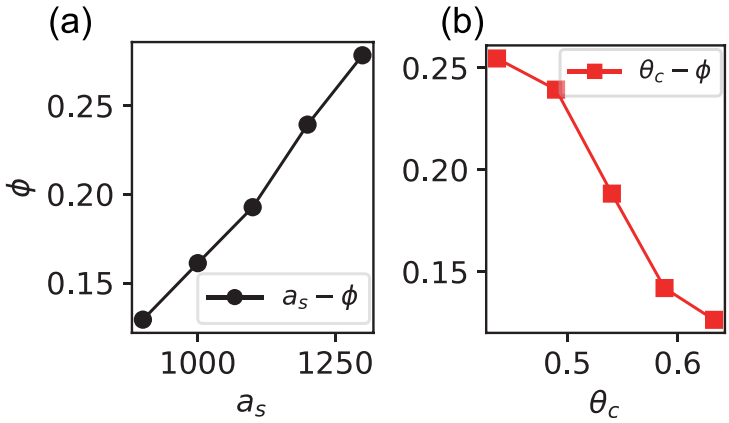

Figure 7. The deflection angle of the x-ray probe varying with (a) different intensities of pump laser a_s, where the collision angle between the pump laser and the probe x-ray is fixed as $\theta_c = 0.489$ rad, (b) different θ_c, where $a_s = 1200$ is fixed.

5. Conclusion

In summary, we have examined the possibility of detecting the vacuum polarization effect based on vacuum refraction and strong lasers. We propose a scheme to explore the quantum vacuum effect on ultraintense laser facilities, in which an x-ray probe laser is applied to obliquely collide with the ultraintense pump laser. The theoretical basis of the scheme is analyzed, where the evolution of the wavefront, intensity, and refraction angle of the probe laser are given. In particular, the refraction angle, which can be served as a detectable signal of the quantum vacuum effect and can be measured under realistic parameters in current experiments. To verify the proposed scheme, a series of 2D PIC simulations, with the vacuum polarization effect self-consistently taken into account, are carried out. The simulation results have confirmed that the generalized Snell's and Fresnel's law can be used as a reasonable description of the refraction of the probe laser for most of the settings that can be employed experimentally today.

Data availability statement

All data that support the findings of this study are included within the article (and any supplementary files).

Acknowledgments

This work is supported by the National Key R&D Program of China (Grants No. 2022YFA1603200, No. 2022YFA1603201); the National Natural Science Foundation of China, Grants No. 11825502, No. 12135001, No. 11921006; the Strategic Priority Research Program of the Chinese Academy of Sciences, Grant No. XDA25050900; B.Q. acknowledges support from the National Natural Sci- ence Funds for Distinguished Young Scholars, Grant No. 11825502.

Appendix A. Wavefront expansion

According to the QED modified Maxwell's equation, the evolution of E can be obtained by

$$\begin{aligned}\partial_t^2\mathbf{E} - c^2\nabla^2\mathbf{E} &= -\hat{\mathbf{e}}_z\partial_t^2 P_z/\varepsilon_0 - \hat{\mathbf{e}}_z\partial_x\partial_t M_y/\varepsilon_0 \\ &= -\hat{\mathbf{e}}_z\partial_t^2\left(A_sB_y - A_sE_z\right) - \hat{\mathbf{e}}_z\partial_x\partial_t\left(A_sE_z - A_sB_y\right).\end{aligned} \tag{A.1}$$

using $-\partial_t\mathbf{B} = \nabla\times\mathbf{E}$, the S-wave propagates in the x, y plane and is uniform along the z direction, we have $\partial_t B_y = \partial_x B_z$. Then in z direction, the evolution of E turns to

$$\begin{aligned}\partial_t^2 E_z - c^2\nabla^2 E_z = A_s\cdot&\left[c\left(\partial_x\partial_t E_z\right) - c^2\left(\partial_x\partial_t B_y\right) - \partial_t^2 E_z + \partial_t^2 B_y\right] \\ &+ \left(\partial_x A_s\right)\left(\partial_t E_z + \partial_t B_y\right) + \left(\partial_t A_s\right)\left(\partial_x E_z + \partial_x B_y + 2\partial_t E_z + 2\partial_t B_y\right) \\ &+ E_z\left(\partial_x\partial_t A_s + \partial_t^2 A_s\right) + B_y\left(\partial_x\partial_t A_s + \partial_t^2 A_s\right).\end{aligned} \tag{A.2}$$

The right hand of equation (A.2) consists of three lines, and we discuss their results in wavefront expansion separately. The first line is represented by $A_s c(\partial_x\partial_t E_z)$ which does not contain a derivative of A_s.

Substitute it into $E_z = \Sigma_{n=0}^{\infty}\phi_n f_n(s) = \Sigma_n \phi_n f_n(t-\sigma(\mathbf{r}))$ and we get

$$c\sum_n \phi_n f_{n-2}\left(-\partial_x\sigma\right)A_s + \partial_x\phi_n f_{n-1}A_s + \phi_n f_{n-1}\partial_x A_s. \tag{A.3}$$

Similarly, substitute the second line represented by $(\partial_t A_s)\partial_x E_z$ which contains the first derivative of A_s to get

$$\sum_n \left(\partial_t A_s\right)\left[\phi_n f_{n-1}\left(-\partial_x\sigma\right) + \left(\partial_x\phi_n\right)f_n\right], \tag{A.4}$$

and substitute the third line represented by $E_z\partial_x\partial_t A_s$ which contains the second derivative of A_s to get

$$\left(\partial_x\partial_t A_s\right)\Sigma_n\phi_n f_n\left(t-\sigma\left(\mathbf{r}\right)\right). \tag{A.5}$$

Generally speaking, we should first equate the coefficient of f_{-2} to 0 to get the equation about σ that is equation (3). Solving for equation (3) determines the evolution of the wavefront. Then, equating the coefficient of f_{-1} leads to the equation about ϕ_0 and σ, thus can determine the ϕ_0. The subsequent coefficients determines $\phi_1, \phi_2, \ldots$, but ϕ_0 is the main quantity that determines the intensity of wavefront.

We can note that since the original equation is a second order derivative equation, $f_{-2} = f_0''$ means that the corresponding coefficient equation (3) does not contain the derivative of A_s. This indicates that equation (3) retains its form in general temporal and spatial nonuniform situations. For the scope of application of equation (3), it requires the convergence of the series of the wavefront expansion. However, the form that f_n takes usually depends on the particular problem, and there is no universally applicable assumption. For example, E_z can be chosen as the expansion form of a power series:

$$E_z = \begin{cases} \phi_0 H(s) + \phi_1 s + \ldots \phi_n \dfrac{1}{n!}s^n + \ldots, s > 0 \\ 0 \qquad\qquad\qquad\qquad ,s < 0 \end{cases} \tag{A.6}$$

where $H(s)$ is Heaviside function. $E_z = 0$ if $s < 0$ indicate that there is no electric field in front of the wavefront ($s = 0$). If E_z takes the form of equation (A.6), then the convergence of the above process holds only for very small s, which only reflects the behavior of the wavefront propagating a small distance. This is sufficient for simple situations, such as the case of the uniform pump field in figure 1, where the wavefront begins to propagate in a straight line after crossing a very small distance from the boundary. However, for more complex pump fields with spatial and temporal variations, the assumption of this power series becomes no longer convenient for larger s. If the frequency of probe laser is high, the typical temporal and spatial scales are $1/\omega, c/\omega$, another commonly used expansion series is

$$E_z = \sum_{n=0}^{\infty}\phi_n\left(x\right)\frac{\mathrm{e}^{-i\omega s}}{\left(-i\omega\right)^n}. \tag{A.7}$$

Thus a simple estimate of magnitude is $f_{n-1} \sim \partial_t f_n(t-\sigma) \sim i\omega f_n$. By comparing the terms $\phi_n f_{n-2}(-\partial_x\sigma)A_s$ and $\phi_n f_{n-1}\partial_x A_s$ in equation (A.3), we can get the conclusion equation (3) is acceptable until $(\phi_n f_{n-1}\partial_x A_s)/(\phi_n f_{n-2}(-\partial_x\sigma)A_s) \sim \frac{c/\omega}{A_s/(\partial_x A_s)} < 1$. This means that under the condition that the variation scale of the pump field is much larger than that of the probe, the equation (3) can be applied in a longer wavefront evolution region. For cases where this condition is not satisfied, it is necessary to rely on the more refined assumption of f_n.

Appendix B. Simulation method

This section includes an explanation of the implementation of the simulation code and some of the operations used in simulations.

PIC program, EPOCH, is an open source program capable of simulating the evolution of EM fields and EM-plasma interactions. It is characterized by user-friendly interaction, reasonable boundary processing and massively parallel computation. Based on the EPOCH framework, the original EM field evolution has been modified from Maxwell's equations to vacuum-polarization-corrected nonlinear Maxwell's equations. More specifically, the modified Maxwell's equations comes from the low-frequency, weak-field limit of the Heisenberg–Euler theory, i.e. leading-order contribution equation (1). This code can directly calculate the macroscopic EM field in both near field and far field, and thus help conveniently deal with problems related to the coherence information of photons [14, 15].

The algorithm we used comes from [52] which is based on the Yee algorithm (a standard second-order fine difference time-domain method). As in the modified Maxwell's equation, the development of EM fields requires the knowledge of future quantities. Therefore, the explicit method the standard Yee algorithm advances EM fields has to be modified. The algorithm we use adds an iteration loop to get a converged result, which is equivalent to an implicit algorithm.

There are two simulation details that need to be mentioned here:

Firstly, there are two forms of adding EM fields in the simulation. The first one is achieved by giving time-dependent value of the boundary EM field, thus realizing the incident laser at the simulated boundary. The pump laser in the collision scenario and all probe lasers and are set in this way. Since in the program, all these EM fields evolutions are based on corrected Maxwell's equations, this guarantees EM fields self-consistency during the evolution. The field value of the boundary-incident laser is set in accordance with the theoretical value of the free vacuum theory. For example, the incident probe laser adopts the form of leading-order paraxial Gaussian beam, thus fulfilling $\mathbf{E}^2-\mathbf{B}^2, \mathbf{E}\cdot\mathbf{B}=0$. The second method is to directly add additional EM fields to the program based on arbitrary time and space distribution functions. This part of the EM field is independent from the self-consistent EM field in the first method in computer memory. This EM field only plays a role in calculating the corresponding polarization vector $\mathbf{P},\mathbf{M}$ in the algorithm, and does not evolve according to Maxwell's equations. This allows us to set the background field very freely, which is reasonable and convenient for exploring the propagation properties of probe laser in different forms of strong background fields. In more practical simulations such as two laser collision case, the pump laser is given in the first method.

Secondly, to demonstrate the vacuum polarization effect within a limited simulation time, we have artificially increased the nonlinear parameter ξ in equation (1). The physical significance of the results remains unaffected by this. Instead, it is merely a proportional adjustment of a constant aimed at emphasizing the effects with greater clarity. This is because the real physical parameter ξ is very small, the effect of vacuum polarization can only consider the part that is proportional to ξ. We provide here a relatively general proof here(in Gaussian units). We denote the pump field as E_s, B_s, probe field as E_p, B_p. Assume that E_{s0}, B_{s0} is the typical amplitude of the pump field, E_0 is the typical amplitude of the probe field and the typical scale of the EM field is described by $x_0=2\pi/k, t_0=2\pi/\omega$. Then, the physical quantity we are concerned about is the electric field of probe laser which can be written as a general form: $E_p=E_0\cdot f(\xi,E_{s0},B_{s0},k,\omega,x,t)$. According to the dimensional analysis (or Buckingham Π theorem, choose E_{s0},x_0,t_0 as the basic units and convert all independent variables in f into dimensionless quantities marked with ~), E_p can be transformed into $E_p=E_0\cdot f(\xi E_{s0}^2,\tilde{B}_{s0},\tilde{x},\tilde{t})$. We also know that when $\xi\to 0$, the equation is only related to $\tilde{x},\tilde{t}$ and can return to the classical limit. So, E_p can be further written as $E_p=E_0\cdot f(h(\xi E_{s0}^2,\tilde{B}_{s0}),\tilde{x},\tilde{t})$. Because the ξ is very small and satisfies $\xi E_{s0}^2\ll 1$, typical value $\tilde{x},\tilde{t}\sim 1$, we can do a Taylor expansion of it to get $E_p=E_0\cdot f_0(x,t)+E_0\cdot f'(\tilde{x},\tilde{t})h'(\tilde{B}_{s0})*\xi E_{s0}^2+o((\xi E_{s0}^2)^2)$. Here, f_0 is the electric field solution of the probe without vacuum polarization effect. This indicates that within this parameter range ($\xi E_{s0}^2\ll 1$) the influence caused by vacuum polarization is proportional to ξ. We arrived at the desired conclusion, and it should be careful to set the magnified ξ to ensure that the term $o((\xi E_{s0}^2)^2)$ is small.

ORCID iDs

G Y Chen https://orcid.org/0000-0002-9537-160X
B F Lei https://orcid.org/0000-0002-3932-6150
S Jin https://orcid.org/0009-0009-8680-9591
B Qiao https://orcid.org/0000-0001-7174-5577

References

[1] Strickland D and Mourou G 1985 *Opt. Commun.* **55** 447–9
[2] ELI delivery consortium | Home (available at: https://eli-laser.eu/)
[3] Facility C L Vulcan (available at: www.clf.stfc.ac.uk/Pages/Vulcan.aspx)
[4] Li W *et al* 2018 *Opt. Lett.* **43** 5681–4
[5] Zavattini G *et al* 2022 *Eur. Phys. J.* C **82** 1–14
[6] Ejlli A, Della Valle F, Gastaldi U, Messineo G, Pengo R, Ruoso G and Zavattini G 2020 *Phys. Rep.* **871** 1–74
[7] Della Valle F, Ejlli A, Gastaldi U, Messineo G, Milotti E, Pengo R, Ruoso G and Zavattini G 2016 *Eur. Phys. J.* C **76** 1–15
[8] Della Valle F, Gastaldi U, Messineo G, Milotti E, Pengo R, Piemontese L, Ruoso G and Zavattini G 2013 *New J. Phys.* **15** 053026
[9] Battesti R *et al* 2008 *Eur. Phys. J.* D **46** 323–33
[10] Cadène A, Berceau P, Fouché M, Battesti R and Rizzo C 2014 *Eur. Phys. J.* D **68** 1–7
[11] Heisenberg W and Euler H 1936 *Z. Phys.* **98** 714–32
[12] Toll J S 1952 *The Dispersion Relation for Light and its Application to Problems Involving Electron Pairs* (Princeton University)
[13] Di Piazza A, Hatsagortsyan K Z and Keitel C H 2006 *Phys. Rev. Lett.* **97** 083603
[14] King B, Di Piazza A and Keitel C H 2010 *Nat. Photon.* **4** 92–94

[15] Kryuchkyan G Y and Hatsagortsyan K Z 2011 *Phys. Rev. Lett.* **107** 053604
[16] Gies H, Karbstein F and Seegert N 2016 *Phys. Rev.* D **93** 085034
[17] Sasorov P, Pegoraro F, Esirkepov T Z and Bulanov S V 2021 *New J. Phys.* **23** 105003
[18] Gies H, Karbstein F and Seegert N 2013 *New J. Phys.* **15** 083002
[19] Gies H, Karbstein F and Seegert N 2015 *New J. Phys.* **17** 043060
[20] Fedotov A, Ilderton A, Karbstein F, King B, Seipt D, Taya H and Torgrimsson G 2023 *Phys. Rep.* **1010** 1–138
[21] Aboushelbaya R *et al* 2019 *Phys. Rev. Lett.* **123** 113604
[22] Mendonça J 2018 *Europhys. Lett.* **120** 61001
[23] Karbstein F 2021 *J. High Energy Phys.* JHEP09(2021)070
[24] Karbstein F and Shaisultanov R 2015 *Phys. Rev.* D **91** 113002
[25] Gies H, Karbstein F and Kohlfürst C 2018 *Phys. Rev.* D **97** 036022
[26] Dinu V, Heinzl T, Ilderton A, Marklund M and Torgrimsson G 2014 *Phys. Rev.* D **89** 125003
[27] Ho W C and Lai D 2003 *Mon. Not. R. Astron. Soc.* **338** 233–52
[28] Sokolova-Lapa E, Stierhof J, Dauser T and Wilms J 2023 *Energy* **1** 10
[29] González Caniulef D, Zane S, Taverna R, Turolla R and Wu K 2016 *Mon. Not. R. Astron. Soc.* **459** 3585–95
[30] Mignani R P, Testa V, Caniulef D G, Taverna R, Turolla R, Zane S, Wu K and Curto G L 2017 arXiv:1710.08709
[31] Zane S and Turolla R 2006 *Mon. Not. R. Astron. Soc.* **366** 727–38
[32] Baring M G and Harding A K 2001 *Astrophys. J.* **547** 929
[33] Pérez-García M, Martínez A P and Querts E R 2022 *Plasma Phys. Control. Fusion* **64** 044011
[34] Heyl J S and Hernquist L 1999 *Phys. Rev.* D **59** 045005
[35] Heinzl T, Liesfeld B, Amthor K-U, Schwoerer H, Sauerbrey R and Wipf A 2006 *Opt. Commun.* **267** 318–21
[36] Bragin S, Meuren S, Keitel C H and Di Piazza A 2017 *Phys. Rev. Lett.* **119** 250403
[37] Karbstein F, Ullmann D, Mosman E A and Zepf M 2022 *Phys. Rev. Lett.* **129** 061802
[38] Karbstein F, Sundqvist C, Schulze K S, Uschmann I, Gies H and Paulus G G 2021 *New J. Phys.* **23** 095001
[39] Grabiger B, Marx-Glowna B, Uschmann I, Loetzsch R, Paulus G G and Schulze K S 2020 *Appl. Phys. Lett.* **117** 201102
[40] Schmitt A T *et al* 2021 *Optica* **8** 56–61
[41] Kim J Y and Lee T 2011 *J. Cosmol. Astropart. Phys.* JCAP11(2011)017
[42] Dobosz M and Iwasinska-Kowalska O 2014 *Appl. Opt.* **53** 111–22
[43] Iwasińska-Kowalska O 2018 *Appl. Opt.* **57** 1417–23
[44] Jones R 1960 *Nature* **186** 706–706
[45] Sarazin X, Couchot F, Djannati-Ataï A, Guilbaud O, Kazamias S, Pittman M and Urban M 2016 *Eur. Phys. J.* D **70** 1–7
[46] Robertson S, Mailliet A, Sarazin X, Couchot F, Baynard E, Demailly J, Pittman M, Djannati-Ataï A, Kazamias S and Urban M 2021 Experiment to observe an optically induced change of the vacuum index *Phys. Rev. A* **103** 023524
[47] Berestetskii V B, Landau L D, Lifshitz E M and Pitaevskii L 1982 *Quantum Electrodynamics* vol 4 (Butterworth-Heinemann)
[48] Schwinger J 1951 *Phys. Rev.* **82** 664
[49] Karbstein F 2020 *Particles* **3** 39–61
[50] Karbstein F 2016 arXiv:1611.09883
[51] Whitham G B 1999 *The Wave equation* (Wiley)
[52] Grismayer T, Torres R, Carneiro P, Cruz F, Fonseca R and Silva L O 2021 *New J. Phys.* **23** 095005
[53] Hu H and Huang J 2014 *Phys. Rev.* A **90** 062111
[54] Dittrich W and Gies H 2000 *Probing the Quantum Vacuum: Perturbative Effective Action Approach in Quantum Electrodynamics and its Application* vol 166 (Springer)